



NRC Publications Archive Archives des publications du CNRC

Numerical Simulation of Turbulent Fluid Flow, Heat and Mass Transfer during Continuous Galvanizing Operations

Ilinca, Florin; Hétu, Jean-François; Ajersch, Frank

This publication could be one of several versions: author's original, accepted manuscript or the publisher's version. /
La version de cette publication peut être l'une des suivantes : la version prépublication de l'auteur, la version
acceptée du manuscrit ou la version de l'éditeur.

Publisher's version / Version de l'éditeur:

*Proceedings of Computational Methods for Coupled Problems in Science and
Engineering, 2005*

NRC Publications Record / Notice d'Archives des publications de CNRC:

<https://nrc-publications.canada.ca/eng/view/object/?id=24f9618d-466b-4ff5-94cc-41ad66b87d79>

<https://publications-cnrc.canada.ca/fra/voir/objet/?id=24f9618d-466b-4ff5-94cc-41ad66b87d79>

Access and use of this website and the material on it are subject to the Terms and Conditions set forth at

<https://nrc-publications.canada.ca/eng/copyright>

READ THESE TERMS AND CONDITIONS CAREFULLY BEFORE USING THIS WEBSITE.

L'accès à ce site Web et l'utilisation de son contenu sont assujettis aux conditions présentées dans le site

<https://publications-cnrc.canada.ca/fra/droits>

LISEZ CES CONDITIONS ATTENTIVEMENT AVANT D'UTILISER CE SITE WEB.

Questions? Contact the NRC Publications Archive team at

PublicationsArchive-ArchivesPublications@nrc-cnrc.gc.ca. If you wish to email the authors directly, please see the
first page of the publication for their contact information.

Vous avez des questions? Nous pouvons vous aider. Pour communiquer directement avec un auteur, consultez la
première page de la revue dans laquelle son article a été publié afin de trouver ses coordonnées. Si vous n'arrivez
pas à les repérer, communiquez avec nous à PublicationsArchive-ArchivesPublications@nrc-cnrc.gc.ca.



National Research
Council Canada

Conseil national de
recherches Canada

Canada

NUMERICAL SIMULATION OF TURBULENT FLUID FLOW, HEAT AND MASS TRANSFER DURING CONTINUOUS GALVANIZING OPERATIONS

Florin Ilinca^{*}, Jean-François Héту^{*} and Frank Ajersch[†]

^{*} Industrial Materials Institute
National Research Council Canada
75 de Mortagne, Boucherville, Québec, Canada, J4B 6Y4
E-mail: florin.ilinca@cnrc-nrc.gc.ca, jean-francois.hetu@cnrc-nrc.gc.ca

[†] École Polytechnique de Montréal
C.P. 6079, Succ. Centre-Ville, Montréal, Québec, Canada, H3C 3A7
Email: frank.ajersch@polymtl.ca

Key words: Galvanizing Bath, Finite Elements, Turbulence, Heat Transfer, Stabilized Methods.

Abstract. *This paper presents the solution of the coupled momentum, heat and mass transfer in order to predict and to better understand the generation and movement of inter-metallic dross particles within a typical galvanizing bath. Solutions for temperature (T), aluminum (Al), and iron (Fe) concentration can be correlated with the solubility limits of Al and Fe to determine the amount of precipitated Al in the form of Fe_2Al_5 top dross. The solution algorithm includes $k-\epsilon$ turbulence modeling for fluid flow, heat and mass transfer, and was adapted for the simulation of a sequence of operating parameters. Turbulence equations are solved for the natural logarithm of the original turbulence variables. This choice results in a major improvement in solution quality (smoothness) and algorithm robustness. The global system of equations describing the unsteady turbulent flow problem is solved in a partly segregated manner. At each time step, global iterations are performed for the momentum-continuity, turbulence, energy and concentration equations. Equations are solved using GLS and GGLS stabilized finite element methods. The numerical model takes into account the effect of inductors, strip movement, immersed hardware and ingot melting. Simulations were carried out over a period of two one-hour cycles having each an ingot-melting period followed by a non-melting period. The paper shows the ability of the proposed algorithm to deal with large applications of industrial relevance and illustrates the cost effectiveness and accuracy of the solution algorithm and of the stabilized finite element methods employed.*

1 INTRODUCTION

Zinc-coated steel is a very important and large-volume product linking steel producers with zinc suppliers across the globe. At present, the steel auto body is still the most cost-effective for conventional production vehicles. About 60% of the world's zinc production is consumed in the fabrication of zinc galvanized products, and this figures is most likely to increase¹. Since the production of high-quality zinc-coated products is a major factor in the

profitability of all steel sheet producers, the technology and quality control of the galvanizing process is of primary concern. Numerical modeling can play an important role in improving the understanding of the process in order to reach an optimum setting of the parameters.

Numerical solutions of the flow regime in a continuous zinc galvanizing operation have been carried out over a number of years in projects sponsored by ILZRO^{2,3} as well as in others studies^{4,5}. The bath configuration consisted of a standard 250 tons pot with a snout angle of 27° and a center back ingot charging system into a holding basket. The previous simulations progressed from laminar to turbulent flow models where the effect of line speed, strip width, induction mixing have all been quantified for isothermal bath conditions operating at steady state. It has become clear that the flow is clearly three dimensional due to the complex geometry of the immersed hardware. This still only simulates the condition for periods of the process when no make up ingots are added to the bath. However, when ingots are added to replace the product layer deposited on the exit sheet, the bath can no longer be considered to be isothermal. During this period the induction-heating rate is increased to adjust to the heat demand of the melting ingot, thereby increasing temperature variations in the bath. The temperature at the inductor exit is higher and the region at the melting surface of the ingot is lower than the average bath temperature. Since the liquid zinc alloy densities are very sensitive to the temperature variations, temperature distribution in the bath affects the overall flow due to natural convection, especially in regions where forced convection is small. This occurs in regions away from the moving strip and immersion rollers⁶. Solution of the thermal field is also important because intermetallic particles of dross (precipitates of Fe_2Al_5) form when the temperature in the zinc bath falls below the solubility limit of the solute components of aluminum and iron in liquid zinc^{7,8}.

The purpose of this present paper is to present a solution algorithm for complex coupled problems and applications to the solution of the flow and heat transfer inside galvanizing baths. The latest numerical simulation methods and high speed processors can now handle very complex flow systems with a very large number of grid points resulting in an extremely detailed prediction of flow. Such a numerical simulation advances the understanding of flow in the galvanizing bath particularly relating to the movement of dross particles in a thermally influenced velocity field. The bath configuration used in the study is the same as was used for the previously reported isothermal calculations³. Heat losses through the pot sidewalls, bottom, and bath surface are taken into account in the heat balance so that the overall average bath temperature remains relatively constant at 460°C. The spatial and temporal distributions of aluminum and iron in the bath are also computed. In view of the transient period of ingot immersion, melting and no ingot addition it becomes essential to model the entire cycle of operation of a normal coating operation. The simulations use industrial data for the melting rate and coating rate to account for the mass balance of the process. A period covering two successive one hour cycles was chosen where the average temperature return to values close to the initial conditions at the start of the cycle, so that the simulations could show the dissolution and transport of the aluminum and iron inside the bath. The solution is obtained for the spatial and temporal distribution of temperature, aluminum and iron content within the bath during a normal galvanizing operation. In order to carry out this task, data on the solubility limits of aluminum and iron with temperature need to be integrated into the solution

in order to distinguish between the amount of dissolved and precipitated aluminum (as Fe_2Al_3) in a typical operation.

In this work solutions of the flow and heat transfer in a galvanizing bath were obtained using a finite-element solution algorithm. The solution algorithm includes k - ϵ turbulence modeling for fluid flow, heat and mass transfer, and was adapted for the simulation of a sequence of operating parameters. Turbulence equations are solved for the natural logarithm of the original turbulence variables. This choice results in a major improvement in solution quality (smoothness) and algorithm robustness. Turbulence variables and source terms in the turbulence equations are represented as the exponential of the computational dependent variables. Hence, all these terms are strictly positive throughout the domain. The change of variables also improves the accuracy in regions of rapid variation of turbulence fields such as boundary layers, stagnation points, and shear layers. The global system of equations describing the unsteady turbulent flow problem is solved in a partly segregated manner. At each time step, global iterations are performed for the momentum-continuity, turbulence, energy and concentration equations. Sub-iterations of turbulence transport equations are also used to accelerate the overall convergence of the iterative process. Equations are solved using GLS and GGLS stabilized finite element methods.

The numerical model takes into account the effect of inductors, strip movement, immersed hardware and ingot melting. Simulations were carried out over a period of two one-hour cycles having each an ingot-melting period followed by a non-melting period. Buoyancy induced flow is especially apparent near the inductors and the melting make up ingot, while little effect is observed in the sheet and rollers region. The presence of an ingot significantly changes the temperature distribution and also results in important variations in the local Al and Fe concentrations since the make up ingot has a higher Al concentration and no Fe. The model also accounts for the Al consumption in the coating and for the Fe dissolution from the steel strip. The simulation showed that during the ingot melting, the total Al concentration is higher at the ingot side of the bath than at the strip exit side. The region below the ingot presents the highest Al concentration whereas lower Al concentrations were found in the region above the sink roll, between the strip and the free surface. It was shown that precipitates form near the ingot surface because this region is surrounded by a solution at lower than average temperature. This information is of major significance in the prediction of the formation of dross particles, which can cause defects on the coated product.

2 PROCESS DESCRIPTION

The modern hot dip galvanizing operation is a complex metallurgical process where steel strip of various width and thickness is continuously coated by rapid immersion in a zinc alloy bath operating at temperature normally between 450 and 480°C. When the steel strip enters the bath an interfacial reaction occurs very rapidly forming an inhibition layer of Fe_2Al_3 . On exiting the bath, the excess solution of zinc is deflected back into the bath by means of air knives, leaving a thin coating. Zinc ingots containing small amounts of Al in solution are periodically added to the bath to maintain a constant bath composition and bath level. The solubility of Al and Fe in the bath is very small and extremely sensitive to temperature. Small

decreases in temperature can precipitate intermetallic solid particles, called dross, which are dispersed with the flow and can eventually be found in the final coating. As a result, the thermal condition of the galvanized bath and its controlled operation is of critical importance for the production of high quality hot dipped galvanized strip of uniform coating thickness and free from defects caused by the presence of dross particles.

A typical galvanizing bath configuration is shown in Figure 1. In section A-A, which is a front view through the symmetry plane, we can see the ingot basket, where the makeup ingots are introduced, the sink, guide and stabilization rolls, the snout, and the moving strip. The present configuration represents a bath of 250 tons of zinc, and 1-ton ingots are added at approximately 1-h intervals. The addition of ingots using a centrally located ingot basket is specific to the Bethlehem Steel works. The snout has the role of protecting the strip at the entry in the bath. At strip exit, air knives control the thickness of the deposition. Two inductors are placed on each side of the bath and are used to maintain the prescribed bath temperature and to ensure an appropriate mixing of the liquid in the bath. Each inductor has two exit sections by which the fluid flows from the inductor to the bath and one entry section by which the fluid flows from the bath to the inductor as seen in section B-B of Figure 1. For each inductor the power setting determines the flow rate and the temperature increase between the inlet and exit sections.

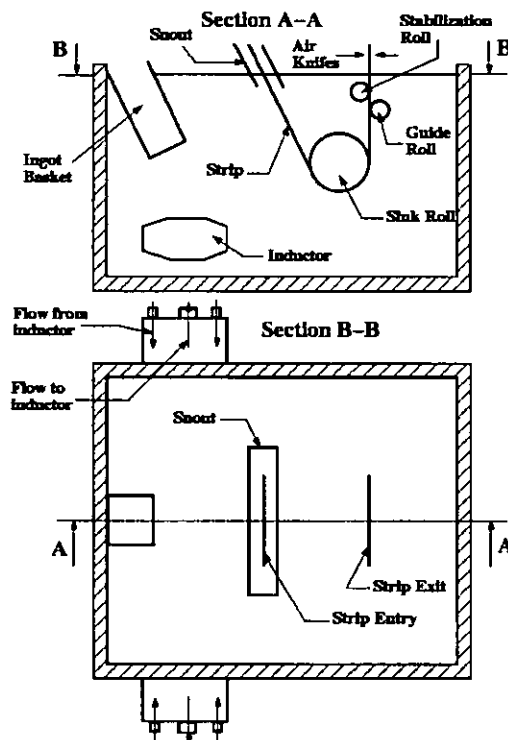


Figure 1: Schematic of a galvanizing bath

3 MATHEMATICAL MODEL

The numerical solution considers a full-scale model of the bath geometry, including all hardware immersed in the bath (sink and stabilizer rolls, roll support arms, snout), two inductors, the ingot basket, and the strip traversing the bath. Given the symmetry of the bath, only one-half is modeled. Simulations consider the density dependence on temperature. Differences in density due to different content in aluminum, which are much smaller compared to those determined by temperature changes, are neglected. The electro-hydrodynamics inside the inductor channels are not modeled, and the flow and temperature increase are imposed as boundary conditions. The quantity of liquid in the bath is considered constant by neglecting the removal of melt as coating on the strip and the addition of material from the ingot, which compensate each other in time. The change of volume of the ingot during melting is not taken into account, and the ingot is considered to occupy the entire volume of the ingot basket. During periods with ingot, the ingot basket surface is considered at the melting temperature, while during periods without ingot, the ingot basket surface is considered insulated.

3.1 Flow and heat transfer equations

Flow inside the bath is described by the incompressible Navier-Stokes equations:

$$\rho \left(\frac{\partial \mathbf{u}}{\partial t} + \mathbf{u} \cdot \nabla \mathbf{u} \right) = -\nabla p + \nabla \cdot [2(\mu + \mu_T) \dot{\gamma}(\mathbf{u})] + \rho \mathbf{g} \quad (1)$$

$$\nabla \cdot \mathbf{u} = 0$$

where $\dot{\gamma}(\mathbf{u}) = (\nabla \mathbf{u} + \nabla \mathbf{u}^T)/2$ is the strain rate tensor, ρ is the density, μ the fluid viscosity, and \mathbf{g} the gravity. When buoyancy effects are neglected, the density is constant, and the gravity term generates just an additional hydrostatic pressure with no influence on the velocity. However, if the density depends on temperature, the gravity term is no longer constant. The usual approximation of buoyancy for small density variations is given by the Boussinesq approximation. Hence, the gravity term is considered as the perturbation from a reference value and the momentum equations become:

$$\rho_0 \left(\frac{\partial \mathbf{u}}{\partial t} + \mathbf{u} \cdot \nabla \mathbf{u} \right) = -\nabla p + \nabla \cdot [2(\mu + \mu_T) \dot{\gamma}(\mathbf{u})] - \rho_0 \mathbf{g} \beta (T - T_0) \quad (2)$$

where ρ_0 is the density at the reference temperature T_0 and β is the thermal expansion coefficient.

Temperature T is obtained by solving the energy equation:

$$\rho c_p \left(\frac{\partial T}{\partial t} + \mathbf{u} \cdot \nabla T \right) = \nabla \cdot [(\lambda + \lambda_T) \nabla T] \quad (3)$$

where c_p is the specific heat, and λ is the thermal conductivity.

Aluminum and iron concentrations c are obtained by solving the mass transport equation:

$$\rho \left(\frac{\partial c}{\partial t} + \mathbf{u} \cdot \nabla c \right) = \nabla \cdot [(D + D_T) \nabla c] \quad (4)$$

where D is the molecular diffusion coefficient. For this work we consider that the Schmidt number $Sc = \mu / D$ is equal to unity. The turbulent diffusion D_T is computed from

$$D_T = \mu_T / Sc_T \quad (5)$$

where Sc_T is the turbulent Schmidt number considered equal to unity.

3.2 Turbulence modeling

The turbulent viscosity μ_T and turbulent conductivity λ_T are computed using the standard $k - \varepsilon$ model of turbulence⁹:

$$\mu_T = \rho C_\mu \frac{k^2}{\varepsilon} \quad (6)$$

$$\lambda_T = \frac{\mu_T C_p}{Pr_T} \quad (7)$$

where Pr_T is the turbulent Prandtl number considered equal to unity.

For this model, the turbulence quantities are the turbulence kinetic energy k and its dissipation rate ε . The transport equations for k and ε are:

$$\rho \left(\frac{\partial k}{\partial t} + \mathbf{u} \cdot \nabla k \right) = \nabla \cdot \left[\left(\mu + \frac{\mu_T}{\sigma_k} \right) \nabla k \right] + P + G - \rho \varepsilon \quad (8)$$

$$\rho \left(\frac{\partial \varepsilon}{\partial t} + \mathbf{u} \cdot \nabla \varepsilon \right) = \nabla \cdot \left[\left(\mu + \frac{\mu_T}{\sigma_\varepsilon} \right) \nabla \varepsilon \right] + C_{\varepsilon 1} \frac{\varepsilon}{k} (P + G) - C_{\varepsilon 2} \rho \frac{\varepsilon^2}{k} \quad (9)$$

where P is the shear production term defined as:

$$P(\mathbf{u}) = \mu_T [\nabla \mathbf{u} : (\nabla \mathbf{u} + \nabla \mathbf{u}^T)] \quad (10)$$

and G accounts for the effect of the buoyancy on the production of turbulence

$$G = \frac{\mu_T}{Pr_T} \beta \mathbf{g} \cdot \nabla T \quad (11)$$

The model constants are⁹: $\sigma_k = 1.0$, $\sigma_\varepsilon = 1.3$, $C_{\varepsilon 1} = 1.44$, $C_{\varepsilon 2} = 1.92$, $C_\mu = 0.09$

3.3 Logarithmic form of the turbulence equations

The turbulence equations in the previous section are notoriously difficult to solve numerically. The eddy viscosity and several source terms contain divisions by the turbulence variables. Negative or small values of the denominator can lead to improper sign or overly large values for μ_T or the source terms. This will cause a dramatic breakdown of the solution algorithm. Enhanced robustness of the algorithm will be achieved if one can ensure that

turbulence variables remain positive throughout the domain and during the course of iterations. One way to preserve positivity of the turbulence variables consists of solving for their logarithms^{10,11}:

$$K = \ln(k), \quad E = \ln(\varepsilon) \quad (12)$$

Solving for K and E guarantees that k and ε will remain positive throughout the computations. Hence the eddy viscosity μ_T will always remain positive. Moreover, solutions from logarithms are more accurate because the fields of the logarithmic variables K and E present smoother variations than those of k and ε ¹¹. The turbulence equations and the eddy viscosity definition for logarithmic variables are as follows:

$$\rho \left(\frac{\partial K}{\partial t} + \mathbf{u} \cdot \nabla K \right) = \nabla \cdot \left[\left(\mu + \frac{\mu_T}{\sigma_k} \right) \nabla K \right] + \left(\mu + \frac{\mu_T}{\sigma_k} \right) (\nabla K)^2 + e^{-K} (P + G) - \rho e^{E-K} \quad (13)$$

$$\rho \left(\frac{\partial E}{\partial t} + \mathbf{u} \cdot \nabla E \right) = \nabla \cdot \left[\left(\mu + \frac{\mu_T}{\sigma_\varepsilon} \right) \nabla E \right] + \left(\mu + \frac{\mu_T}{\sigma_\varepsilon} \right) (\nabla E)^2 + C_{e1} e^{-K} (P + G) - C_{e2} \rho e^{E-K} \quad (14)$$

$$\mu_T = \rho C_\mu e^{2K-E} \quad (15)$$

3.4 Boundary conditions

Boundary conditions for the momentum equations are specified on the strip and the inlet section (inductor inlet) as well as on the solid boundaries (walls). The inductor inlet has been modeled using a flow rate correlated to the inductor power (400 kW at maximum capacity). The influence of the inductor itself has been introduced through Dirichlet boundary conditions (prescribed velocities). Boundary conditions imposed on the Navier-Stokes equations are then as follow:

$$\left. \begin{aligned} \mathbf{u} &= \mathbf{U}_{inductor} && \text{on } \Gamma_{inductor inlet} \\ 2(\mu + \mu_T) \nabla(\mathbf{u} - \mathbf{u}_w) \cdot \mathbf{n} - p \mathbf{n} &= \boldsymbol{\tau}_w \\ \mathbf{u} \cdot \mathbf{n} &= 0 \end{aligned} \right\} \text{on } \Gamma_{wall} \text{ and } \Gamma_{strip} \quad (16)$$

where $\begin{cases} \mathbf{u}_w = 0 & \text{on } \Gamma_{wall} \\ \mathbf{u}_w = \mathbf{u}_{strip} & \text{on } \Gamma_{strip} \end{cases}$

A velocity wall function is applied on all mobile and immobile surfaces, e.g. bath walls, strip, rollers, snout and arms. The wall function correlates the tangential stresses in the boundary layers to the relative tangential velocity.

$$\boldsymbol{\tau}_w = - \frac{\rho C_\mu^{1/4} k_w^{1/2}}{U^+} (\mathbf{u} - \mathbf{u}_w) \quad (17)$$

where

$$U^+ = \begin{cases} y^+ & , y^+ < y_c^+ \\ \frac{1}{\kappa} \ln(E y^+) & , y^+ \geq y_c^+ \end{cases} \quad (18)$$

$$y^+ = \frac{\rho C_\mu^{1/4} k_w^{1/2} y}{\mu}$$

Here u_w is the velocity at the wall, y is the distance between the computational boundary and the wall, κ is the Von Karman constant ($\kappa=0.41$) and E is a roughness parameter ($E=9.0$ for smooth walls). The normal derivative of the turbulence kinetic energy is set to zero near the wall so that its values at boundary points k_w are computed implicitly. Then the turbulence dissipation ε at the wall is obtained by using

$$\varepsilon_w = \frac{C_\mu^{3/4} k_w^{3/2}}{\kappa y} \quad (19)$$

The velocity is constrained to be tangent to the wall by imposing the normal velocity to be zero. It is also assumed that the position of the top surface remains at the same height. The regions of the top surface inside the snout and close to the strip exit are considered as free surfaces and only the normal component of the velocity is set to zero. The remaining regions on the top surface were considered covered by solidified zinc oxide and treated as solid walls.

The temperature boundary conditions at a wall are enforced by a temperature wall function¹². The procedure is similar to that used for the velocity and consists in imposing a wall heat flux given by

$$q_w = h_T (T - T_w) \quad (20)$$

$$h_T = \frac{\rho C_p C_\mu^{1/4} k_w^{1/2}}{T^+} \quad (21)$$

where T_w is the wall temperature and T^+ is function of y^+ (see Ignat *et al.*¹² for more details). When the ingot is present in the bath T_w on the ingot surface is considered equal to the melting temperature ($T_w=420^\circ\text{C}$). On the bath walls, in addition to the temperature wall function, boundary conditions take into account the heat loss through walls. This is modeled using a convection boundary condition

$$q_w = h_c (T_w - T_a) \quad (22)$$

where h_c is a heat transfer coefficient and T_a is the ambient temperature. The wall function coupled with the convection heat transfer through walls results in a wall heat flux given by

$$q_w = h(T - T_a) \quad (23)$$

in which h is an equivalent heat transfer coefficient, $h = h_T h_c / (h_T + h_c)$.

For the aluminum and iron transport in the bath the boundary and initial conditions must also be imposed for the aluminum and iron concentrations. The initial aluminum concentration in the bath is considered 0.14% in weight and the bath is considered saturated in Fe at the initial temperature of 460°C. The limit of solubility is given by¹³:

$$\left(\frac{C_{Fe}}{100}\right)^2 \left(\frac{C_{Al}}{100}\right)^5 = \exp\left(0.064 - \frac{36133}{T + 273}\right) \quad (24)$$

where C_{Fe} , C_{Al} are the weight concentrations of Fe and Al expressed in percentage (quantity in kg of Al or Fe for 100kg of solution), and T is the temperature in °C.

On the bath walls we impose a zero normal mass flux for aluminum and iron concentrations (no generation or consumption). The boundary conditions take into account the additional aluminum from the ingot and the aluminum consumption on the steel strip. Since ingots are added to the bath at ambient temperature, no aluminum is transferred to the bath until the ingot reaches the melting point. This was found to take six minutes¹⁴. The melting time is therefore 14 minutes during which all the aluminum and zinc in the ingot is transferred in the bath. Hence the effective ingot mass flux is:

$$(q_{Al})_{ingot} = \begin{cases} 0 & , t < t_1 \\ q_{Al}^* \left[1 - \frac{(t - t_1)^2}{(t_2 - t_1)^2} \right] & , t_1 < t < t_2 \end{cases} \quad (25)$$

with $t_1=6\text{min}$ and $t_2=20\text{min}$ (see Figure 2), and q_{Al}^* is the initial flux of Al at $t=6\text{min}$ which is 2.143 times the average Al flux calculated for a total melting time of 20 minutes. The mass flux on the ingot surface for the iron concentration equation takes into account the fact that the ingot has no iron in its composition.

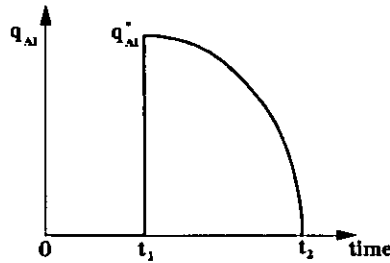


Figure 2: Time evolution of the aluminum flux on the ingot surface

Aluminum consumption on the strip surface is assumed to take place on the first 0.35m of the strip from his entry on the bath (corresponding to 0.2sec. at a strip velocity of 1.75m/s). The overall aluminum concentration of the coating is considered to be 0.4% by weight for a coating weight of 60g/m² (0.06kg/m²) per side. The mean aluminum consumption flux is given by:

$$(q_{Al})_{strip} = -\frac{0.06 \text{ kg/m}^2}{0.35 \text{ m}} v_{strip} c_{Al} \quad (26)$$

The mass flux is $(q_{Al})_{strip} = -0.3 c_{Al} \text{ kg/(m}^2\text{s)}$ for a strip velocity of 1.75m/s, with $c_{Al} = 0.4$. Similarly, an iron mass flux is imposed on the strip surface to take into account for the iron dissolution. The iron dissolution rate was considered at 120 mg/m² of coil¹⁵.

Since the aluminum and iron solubility in the bath varies with temperature as given by eq. (24), any excess aluminum will be present in form of precipitates of Fe₂Al₃ (top dross). Both dissolved aluminum and precipitated aluminum were calculated.

4 FINITE ELEMENT SOLUTION

The global system of equations is solved in a partly segregated manner.^{6,16} The solution algorithm is illustrated in Figure 3.

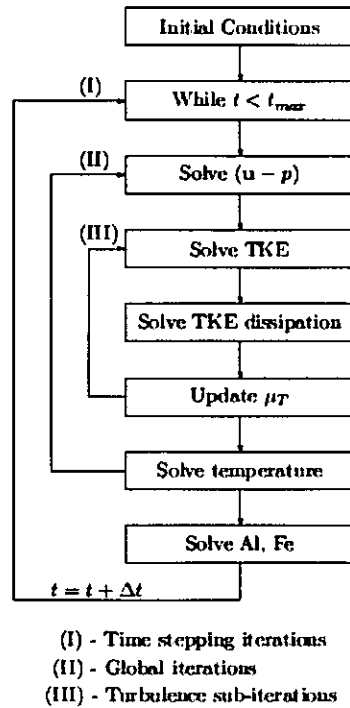


Figure 3: Solution algorithm

At each time step, global iterations are performed for the momentum-continuity, turbulence, and energy equations. Generally, at each time step three global iterations are sufficient to reach satisfactorily converged solutions. Sub-iterations of turbulence transport equations are also used to accelerate the overall convergence of the iterative process. Time

derivatives are discretized by an implicit Euler scheme. Equations are solved by stabilized finite element formulations as described hereafter.

4.1 Momentum-continuity equations

The momentum-continuity equations are solved by using the GLS stabilized finite element method^{17,18}:

$$\begin{aligned} & \int_{\Omega} \rho_0 \left(\frac{\mathbf{u} - \mathbf{u}_0}{\Delta t} + \mathbf{u} \cdot \nabla \mathbf{u} \right) \mathbf{v} d\Omega - \int_{\Omega} p \nabla \cdot \mathbf{v} d\Omega + \int_{\Omega} 2(\mu + \mu_T) \dot{\gamma}(\mathbf{u}) : \dot{\gamma}(\mathbf{v}) d\Omega + \int_{\Omega} \rho_0 \mathbf{g} \beta (T - T_0) \mathbf{v} d\Omega + \int_{\Omega} \nabla \cdot \mathbf{u} q d\Omega \\ & + \sum_K \int_{\Omega_K} \left\{ \rho_0 \left(\frac{\mathbf{u} - \mathbf{u}_0}{\Delta t} + \mathbf{u} \cdot \nabla \mathbf{u} \right) + \nabla p - \nabla \cdot [2(\mu + \mu_T) \dot{\gamma}(\mathbf{u})] + \rho_0 \mathbf{g} \beta (T - T_0) \right\} \tau_u (\rho_0 \mathbf{u} \cdot \nabla \mathbf{v} + \nabla q) d\Omega_K = 0. \end{aligned} \quad (27)$$

The stabilization parameter τ_u is defined as:

$$\tau_u = \left[\left(\frac{2\rho_0 |\mathbf{u}|}{h_K} \right)^2 + \left(\frac{4(\mu + \mu_T)}{m_k h_K^2} \right)^2 + \left(\frac{\rho_0}{\Delta t} \right)^2 \right]^{-1/2}, \quad (28)$$

where h_K is the size of the element K and m_k is a coefficient commonly taken 1/3 for linear elements.

The GLS method contains additional stabilization terms providing smooth solutions to convection-dominating flows. This method also deals with velocity-pressure coupling so that equal-order interpolation results in a stable numerical scheme. This allows the use of simple linear elements for velocity and pressure.

4.2 Energy and concentration equations

The energy and concentration equations are dominated by the convective term. Therefore the SUPG method¹⁸ is appropriate. The variational formulation for the energy equation is as follows:

$$\begin{aligned} & \int_{\Omega} \rho c_p \left(\frac{T - T_0}{\Delta t} + \mathbf{u} \cdot \nabla T \right) w d\Omega + \int_{\Omega} (\lambda + \lambda_T) \nabla T \cdot \nabla w d\Omega \\ & + \sum_K \int_{\Omega_K} \left\{ \rho c_p \left(\frac{T - T_0}{\Delta t} + \mathbf{u} \cdot \nabla T \right) - \nabla \cdot [(\lambda + \lambda_T) \nabla T] \right\} \tau_T (\rho c_p \mathbf{u} \cdot \nabla w) d\Omega_K = 0. \end{aligned} \quad (29)$$

The stabilization parameter τ_T is defined as:

$$\tau_T = \left[\left(\frac{2\rho c_p |\mathbf{u}|}{h_K} \right)^2 + \left(\frac{4(\lambda + \lambda_T)}{m_k h_K^2} \right)^2 + \left(\frac{\rho c_p}{\Delta t} \right)^2 \right]^{-1/2}. \quad (30)$$

4.3 Turbulence equations

Turbulence equations are solved by a Streamline Upwind Petrov-Galerkin / Galerkin Gradient Least-Squares (SUPG/GGLS) method.^{18,19,20} The SUPG contribution to the stabilization deals with the convective term, while the GGLS contribution stabilizes for the source terms. The stabilized formulation is shown here for the equation for K (the logarithm of turbulence kinetic energy):

$$\begin{aligned} & \int_{\Omega} \rho \left(\frac{K - K_0}{\Delta t} + \mathbf{u} \cdot \nabla K \right) w d\Omega + \int_{\Omega} \left(\mu + \frac{\mu_T}{\sigma_k} \right) \nabla K \cdot \nabla w d\Omega - \int_{\Omega} \left[\left(\mu + \frac{\mu_T}{\sigma_k} \right) (\nabla K)^2 + e^{-K} (P + G) - \rho e^{E-K} \right] w d\Omega \\ & + \sum_K \int_{\Omega_K} \left\{ \rho \left(\frac{K - K_0}{\Delta t} + \mathbf{u} \cdot \nabla K \right) - \nabla \cdot \left[\left(\mu + \frac{\mu_T}{\sigma_k} \right) \nabla K \right] - \left(\mu + \frac{\mu_T}{\sigma_k} \right) (\nabla K)^2 - e^{-K} (P + G) + \rho e^{E-K} \right\} \tau_K (\rho \mathbf{u} \cdot \nabla w) d\Omega_K \\ & + \sum_K \int_{\Omega_K} \nabla \cdot \left\{ \rho \left(\frac{K - K_0}{\Delta t} + \mathbf{u} \cdot \nabla K \right) - \nabla \cdot \left[\left(\mu + \frac{\mu_T}{\sigma_k} \right) \nabla K \right] - \left(\mu + \frac{\mu_T}{\sigma_k} \right) (\nabla K)^2 - e^{-K} (P + G) + \rho e^{E-K} \right\} \tau_K \nabla w d\Omega_K = 0. \end{aligned} \quad (31)$$

The stabilization parameter τ_K of the SUPG stabilization term is given by:

$$\tau_K = \left[\left(\frac{2\rho|\mathbf{u}|}{h_K} \right)^2 + \left(\frac{4(\mu + \mu_T / \sigma_k)}{m_k h_K^2} \right)^2 + \left(\frac{\rho}{\Delta t} \right)^2 \right]^{-1/2}, \quad (32)$$

whereas $\tau_{\nabla K}$ is given by:

$$\tau_{\nabla} = \frac{h_K^2}{6} \bar{\xi}, \quad (33)$$

$$\bar{\xi} = \frac{\cosh(\sqrt{6\alpha}) + 2}{\cosh(\sqrt{6\alpha}) - 1} - \frac{1}{\alpha}, \quad (34)$$

$$\alpha = \frac{(\rho / \Delta t) h_K^2}{6(\mu + \mu_T / \sigma_k)}. \quad (35)$$

In this work linear elements are used and therefore several terms in equation (31) vanish. The resulting stabilized finite element equation is as follows:

$$\begin{aligned} & \int_{\Omega} \rho \left(\frac{K - K_0}{\Delta t} + \mathbf{u} \cdot \nabla K \right) w d\Omega + \int_{\Omega} \left(\mu + \frac{\mu_T}{\sigma_k} \right) \nabla K \cdot \nabla w d\Omega - \int_{\Omega} \left[\left(\mu + \frac{\mu_T}{\sigma_k} \right) (\nabla K)^2 + e^{-K} (P + G) - \rho e^{E-K} \right] w d\Omega \\ & + \sum_K \int_{\Omega_K} \left\{ \rho \left(\frac{K - K_0}{\Delta t} + \mathbf{u} \cdot \nabla K \right) - \left(\mu + \frac{\mu_T}{\sigma_k} \right) (\nabla K)^2 - e^{-K} (P + G) + \rho e^{E-K} \right\} \tau_K (\rho \mathbf{u} \cdot \nabla w) d\Omega_K \\ & + \sum_K \int_{\Omega_K} \left\{ \rho \left(\frac{\nabla K - \nabla K_0}{\Delta t} \right) + e^{-K} \nabla K (P + G) + \rho e^{E-K} \nabla (E - K) \right\} \tau_K \nabla w d\Omega_K = 0. \end{aligned} \quad (36)$$

5 NUMERICAL RESULTS

Computations were carried out on a cluster of Pentium III processors running at 1 GHz, connected by a 100 Mbps-Fast Ethernet network. The transient solution for a time interval of 120 minutes (720 time steps of 10 seconds each) is computed in about 36 hours. For the present case the computational mesh has 1,106,928 tetrahedral elements and 191,162 nodes.

The volumetric regions where the zinc flows at a speed lower than 0.01m/s are illustrated in Figure 4. The small velocities are localized in a few stagnation regions inside the bath. When increasing the power to the inductors (a), the small velocity region decreases and, as expected, most of the differences occur near the exit from the inductors. Also, the presence of the cold ingot results in the formation of a strong recirculating region between the ingot and inductors (left hand side of the bath), further reducing the size of the small velocity region.

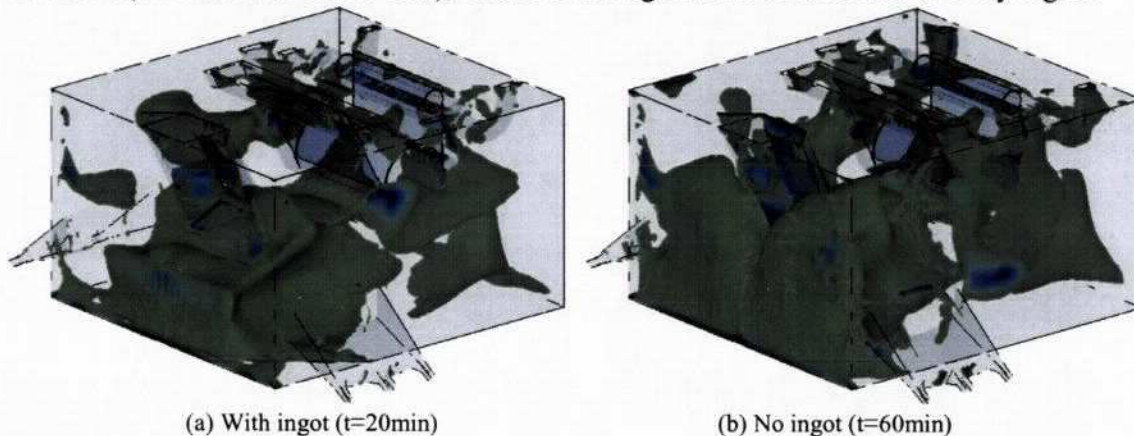


Figure 4: Volume with velocity smaller than 0.01m/s

Figure 5 shows the distribution of temperature on the symmetry plane. With ingot present, the cold zinc melting from the ingot flows to the bottom of the bath and the solution presents higher temperature gradients than for the case without ingot. Figure 6 illustrates the distribution of total aluminum concentration on the symmetry plane with and without ingot. With ingot present, we observe a higher level of aluminum near the ingot and a lower level of aluminum near the strip entry where aluminum consumption takes place. Without ingot, the aluminum concentration becomes very uniform except for a region near the strip entry point where the aluminum concentration is smaller. These results are in agreement with the global mass exchange that is driven by aluminum addition from the ingot and aluminum consumption during the formation of the inhibition layer in the region near the entry of the strip. Similar results are shown in Figure 7 for the iron concentration, this time the region under the melting ingot having lower iron concentration because the ingot has no iron, while around the strip entry point iron concentration is larger because of the iron dissolution that occurs before the formation of the inhibition layer. At the end of the cycle (60min) the iron concentration is relatively uniform with a slightly higher concentration close to the strip near his entry point due to iron dissolution from the strip.

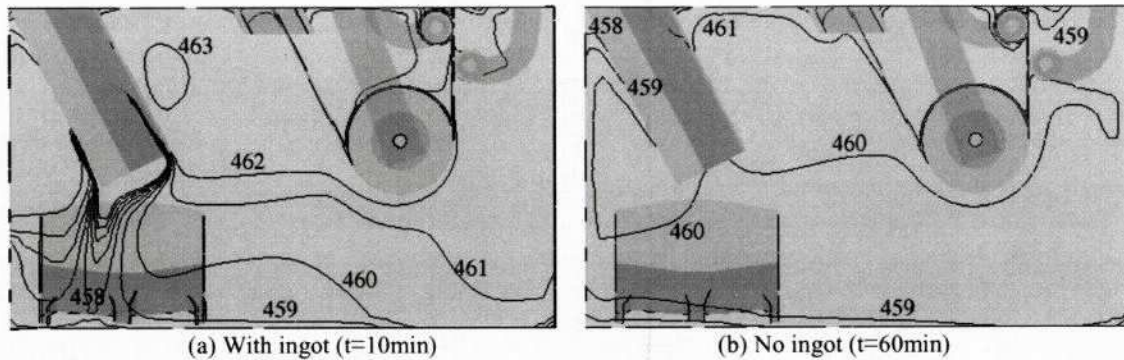


Figure 5: Temperature distribution on the symmetry plane: (a) with ingot ($t=10\text{min}$) and (b) no ingot ($t=60\text{min}$) (increment between iso-values is 1°C)

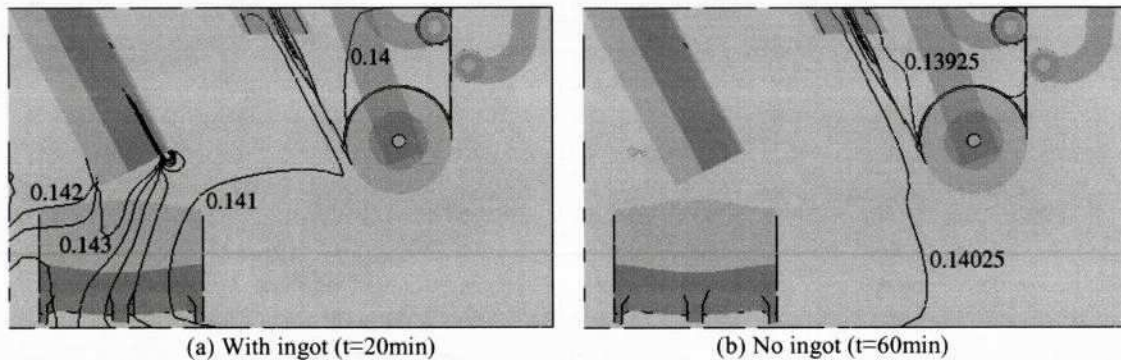


Figure 6: Total aluminum concentration on the symmetry plane: (a) with ingot ($t=20\text{min}$), (b) no ingot ($t=60\text{min}$) (increment between iso-values is 0.0005)

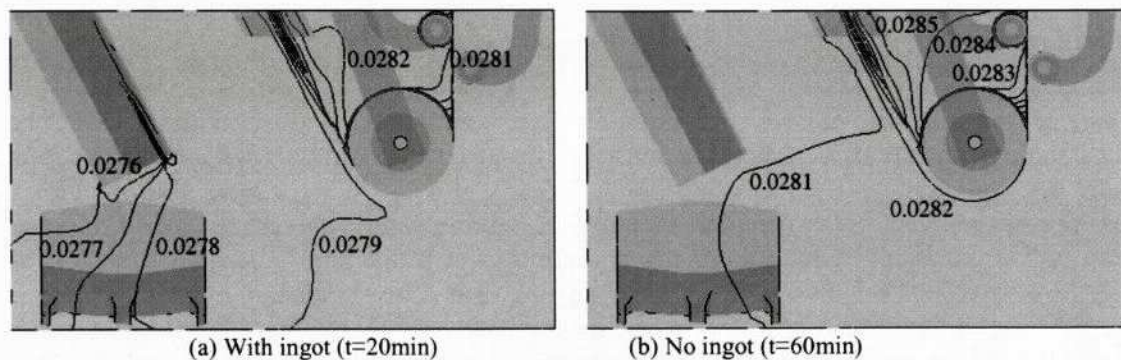


Figure 7: Total iron concentration on the symmetry plane: (a) with ingot ($t=20\text{min}$), (b) no ingot ($t=60\text{min}$) (increment between iso-values is 0.0001)

In order to illustrate the evolution of different variables during two complete cycles of 20min with ingot melting and 40min without ingot, graphs were plotted for 4 specific locations in the bath on the ingot side, for 4 locations on the strip exit side and for 4 locations inside the snout. These locations are illustrated in Figure 8.

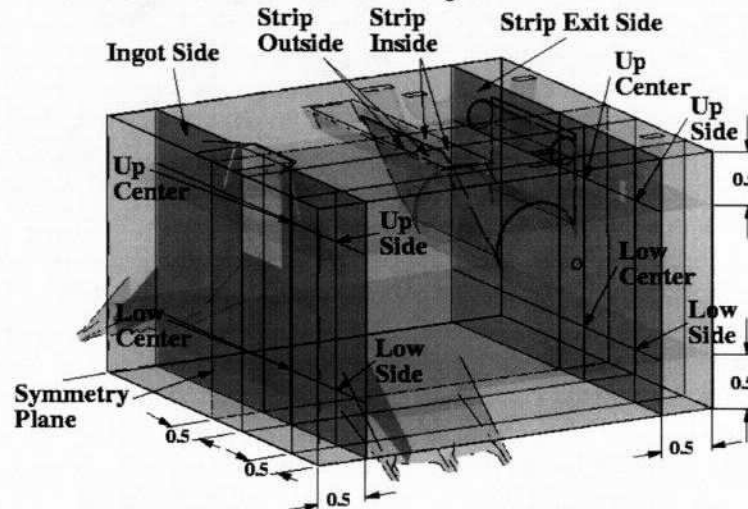


Figure 8: Location of points for plots in time (dimensions are in meters)

Figure 9 illustrates the evolution in time of the temperature (left) and total aluminum (right) over two complete cycles. The initial temperature is uniform at 460°C. As soon as the ingot is introduced into the bath ($t=0$) the temperature drops at the inductor/ingot side at the Low-Left and Low-Right locations. The temperature rises at the Up-Right location because inductors are running at higher power projecting heated zinc towards the top surface of the bath. We can also observe that the temperature gradients are higher on the ingot side and during the ingot-melting period ($t=0-20\text{min}$). Without ingot, the temperature becomes more uniform with an initial correction between $t=20\text{min}$ and $t=30\text{min}$. The stratification of temperature in the bath is due to buoyancy. On the strip exit side and inside the snout the temperature is more uniform and varies as the mean temperature. During the period at 100% inductor power the temperature increases by 3-4 degrees and decreases back to a temperature close to the initial temperature during the period with no ingot in the bath.

The evolution in time of the total aluminum concentration is shown in the right hand side of Figure 9. The total aluminum represents the amount that is in solution as well as the amount that is in precipitated form. Subsequent calculations to differentiate between the dissolved and precipitated form of aluminum assume that the rate of dissolution and precipitation are instantaneous. The initial aluminum concentration is 0.14 wt% ($t=0$). During the first 6min the ingot is brought up to the melting point. During this period the aluminum concentration decreases, especially near the strip, as aluminum consumption takes place on the strip without any supply from the ingot. When the ingot begins to melt ($t=6\text{min}$) a sharp increase of aluminum concentration is observed on the ingot side. On the strip exit side the

increase is delayed by about 3 min, corresponding to the time it takes for the zinc on the ingot side to reach the front (strip section) of the bath as a result of the overall bath flow. Validation tests using aluminum sensors to measure the variations in aluminum level after the addition of brightener bars presented in a previous study³ observed nearly the same value of the time increment. During ingot melting the total aluminum concentration in the bath is higher, with a maximum value near the ingot at about $t=14\text{min}$. On the ingot side the differences between different locations are more apparent resulting in larger values on the Low-Left location and the lowest values for the Up-Left location. Flow from the ingot (rich in aluminum) reaches the Low-Left location first, followed by the Low-Right, Up-Right, and finally Up-Left locations. This is in good agreement with the buoyancy driven movement of zinc⁶. On the strip exit side the aluminum concentration is more uniform, since this area is mixed at a much higher intensity due to the roll and strip movement. Without ingot, the aluminum concentration becomes more uniform but still remains higher on the ingot side. During this period the aluminum concentration decreases constantly because of the aluminum consumption on the strip. Inside the snout, uniform aluminum concentration is observed except for the region near the center of the inner side of the strip. This is indicative of a zone that does not readily mix with the zone in contact with the external side of the strip. In industrial practice however, very little difference is observed in the total aluminum content of the coatings on either side of the strip. The small differences of aluminum content in the regions of the bath in contact with the inner and outer surface of the strip do not seem to affect the total amount of aluminum to the overall coating.

Figure 10 shows the evolution in time of the total iron concentration. Iron concentration increases throughout the operation due to iron dissolution from the strip, except for a small period during ingot melting when material with no iron content is introduced in the bath. Iron concentration is close to uniform with the point inside the snout near the center of the inner side of the strip having a larger concentration because of iron dissolution and poor mixing. The initial iron concentration corresponds to the limit of solubility of aluminum and iron for 0.14 wt% Al content at the initial temperature of 460°C and the total increase in the iron content is of only about 0.0005 wt% over two cycles.

The concentration of aluminum precipitated as Fe_2Al_3 dross is shown in the right hand side of Figure 10. This value is determined as the mass of aluminum above the temperature dependent limit of solubility. When the ingot is immersed we observe a sharp increase in dross formation on the ingot side. This is caused by the decrease in temperature, which is highest at the Low-Left location. During ingot melting dross is also formed as the aluminum rich ingot dissolves in the bath. The ingot melting determines the formation of dross only in the region around the ingot. Finally dross is also formed at the end of the cycle because of the overall decrease in temperature. The numerical model clearly indicates that larger variations are observed on the ingot side. Dross is formed mostly at the bottom of the bath where the temperature is lower. The calculations also show that smaller quantities of dross are formed inside the snout representing only a very small fraction of the total dross formed.

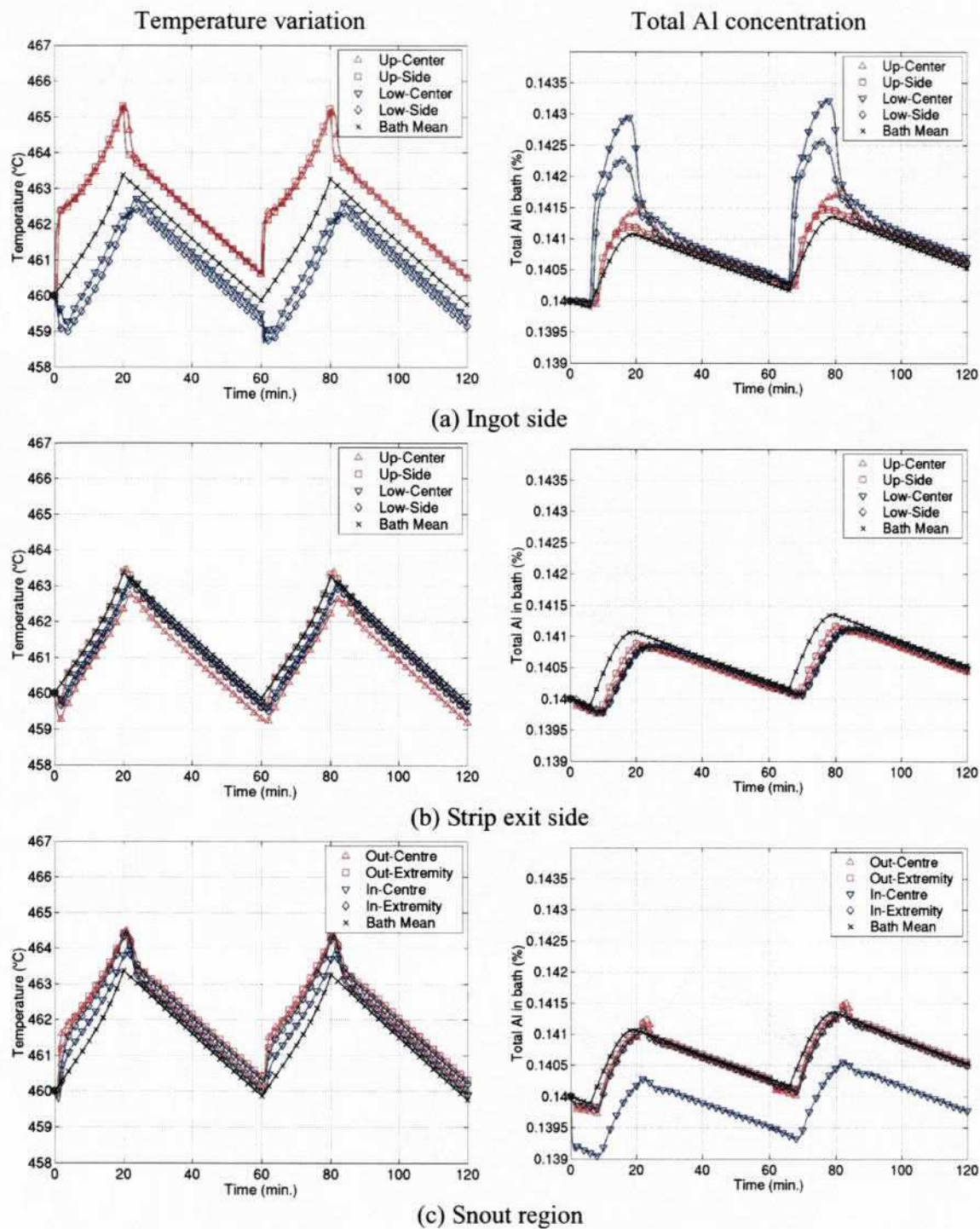


Figure 9: Temperature and total Al history during two complete cycles

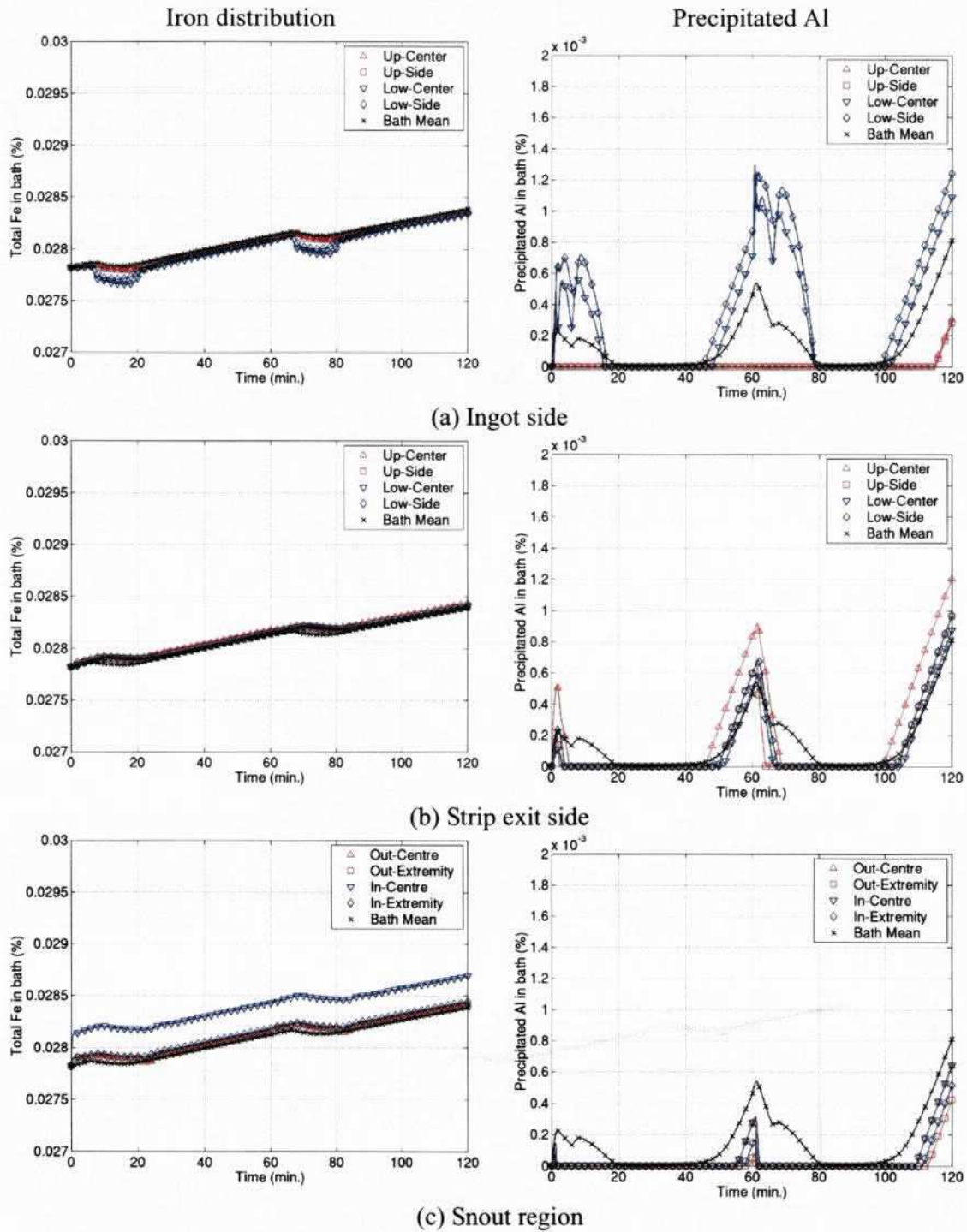


Figure 10: Iron and precipitated Al history during two complete cycles

7 CONCLUSIONS

This article presented a solution algorithm for the turbulent flow, heat and mass transfer in a galvanizing bath. The numerical simulations carried out in this paper show the spatial and temporal distribution of aluminum and iron content in a typical galvanizing bath during a sequence of ingot addition and melting followed by a period when no ingot is present in the bath. The numerical model accounted for the effect of inductors, strip movement, immersed hardware and ingot melting. Turbulence equations are solved for the logarithms of turbulence variables resulting in increased robustness and accuracy of the solution. The algorithm is segregated, solving separately the momentum-continuity, turbulence, energy, and concentration equations by using stabilized finite element methods. At each time step three global iterations were sufficient to reach satisfactorily converged solutions. The paper illustrated the ability of the proposed algorithm to deal with such a large industrial application. The procedure is cost effective and results in accurate numerical solutions, which agree well with experimental observations.

8 ACKNOWLEDGEMENTS

The authors would like to acknowledge particularly Dr. F.E. Goodwin, the International Lead Zinc Research Organization (ILZRO) and the industrial sponsors for funding this project. The authors also wish to acknowledge the contribution of Michel Perrault in creating the bath mesh for the simulation.

REFERENCES

- [1] F. Ajersch, M. Gauthier, and C. Binet, "Kinetics of continuous galvanizing process," in *Fundamentals of Metallurgical Processing - J.M. Toguri Symposium*, G. Kaiura, C. Pickles, T. Utigard, and A. Vahed, eds., 161-178 (2000).
- [2] A. Paré, C. Binet, F. Ajersch, "Numerical simulation of 3-D flow in a continuous strip galvanizing bath," in *GALVATECH '95 (Iron & Steel Society, ed.)*, 695-706 (1995).
- [3] F. Ajersch, C. Binet, F.E. Goodwin, K.S. Turke, P.S. Kolisuyk, "Validation studies of the numerical simulation of flow in the Bethlehem Steel, Burns Harbor galvanizing bath," in *GALVATECH '98 (Iron & Steel Inst. of Japan, ed.)*, 642-647 (1998).
- [4] M. Gagné, M. Gang: "Numerical modeling of fluid flow pattern in a continuous galvanizing bath," in *GALVATECH '98 (Iron & Steel Inst. of Japan, ed.)*, 90-95 (1998).
- [5] K. Otsuka, M. Arai, S. Kasai: "Development of dross control methods in a continuous galvanizing pot by numerical bath flow analysis," in *GALVATECH '98 (Iron & Steel Inst. of Japan, ed.)*, 96-101 (1998).
- [6] F. Ilinca, J.-F. Héту, F. Ajersch: "Three-dimensional numerical simulation of turbulent flow and heat transfer in a continuous galvanizing bath," *Num. Heat Trans., Part A: Appl.*, **44**, 463-482 (2003).
- [7] F. Ajersch, L. Trépanier, and F.E. Goodwin, "Particle size and composition of dross particles from galvanize and galvaneal operations," *44th MWSP Conference Proceedings (Iron and Steel Society, eds.)* **XL**, 771-780 (2002).
- [8] Y.H. Liu, N.-Y. Tang, L. Zhang, S.G. Denner, and F.E. Goodwin, "Dross formation and

- control during transition from galvannealing to galvanizing," *44th MWSP Conference Proceedings (Iron and Steel Society, eds.)*, **XL**, 781-790 (2002).
- [9] B.E. Launder, D.B. Spalding: "Mathematical Models of Turbulence," 6th ed., Acad. Press, London (1972).
- [10] F. Ilinca, "Méthodes d'éléments finis adaptatives pour les écoulements turbulents," PhD thesis, École Polytechnique of Montréal, March 1996.
- [11] F. Ilinca and D. Pelletier, "Positivity preservation and adaptive solution for the k- ϵ model of turbulence," *AIAA Journal*, **36**(1), 44-50 (1998).
- [12] L. Ignat, D. Pelletier, F. Ilinca: "Adaptive computations of turbulent forced convection," *Num. Heat Trans. Part A*, **34**, 847-871 (1998).
- [13] N.-Y. Tang, "Refined 450°C isotherm of Zn-Fe-Al phase diagram," *Mat. Sc. Tech.*, **11**, 870-873 (1995).
- [14] P. Toussaint, Ph. Vermin, L. Segers, R. Winand, and M. Dubois, "Experimental study and mathematical modeling of zinc ingot melting behavior in continuous hot dip galvanizing process," *Ironmaking and Steelmaking*, **22**, 171-176 (1995).
- [15] Thinh Le, M. Gagné, "Material balance in the zinc bath at Dofasco no. 4 CGL," in *GALVATECH '01 (Iron & Steel Society, ed.)*, 533-539 (2001).
- [16] F. Ilinca and J.-F. Héту, "Finite element solution of three-dimensional turbulent flows applied to mould-filling problems," *Int. J. Numer. Meth. Fluids*, **34**, 729-750 (2000).
- [17] T.J.R. Hughes, L.P. Franca, G.M. Hulbert, "A new finite element formulation for computational fluid dynamics: VII. The Galerkin-Least-Squares method for advective-diffusive equations," *Comp. Methods in Applied Mech. and Engng.*, **73**, 173-189 (1989).
- [18] L.P. Franca and S.L. Frey, "Stabilized finite element methods: {II.} The incompressible Navier-Stokes equations," *Comp. Methods in Applied Mech. and Engng.*, **99**, 209-233 (1992).
- [19] L.P. Franca and E.G. Dutra Do Carmo, "The Galerkin gradient least-squares method," *Comp. Methods in Applied Mech. and Engng.*, **74**, 41-54 (1989).
- [20] F. Ilinca, and J.-F. Héту, "Galerkin gradient least-squares formulations for transient conduction heat transfer," *Comp. Methods in Applied Mech. and Engng.*, **191**, 3073-3097 (2002).